



Facile synthesis of sludge-derived MnO_x -N-biochar as an efficient catalyst for peroxymonosulfate activation

Md Manik Mian^{a,b}, Guijian Liu^{a,b,*}, Biao Fu^{a,b}, Yu Song^{a,b}

^a CAS Key Laboratory of Crust-Mantle Materials and the Environments, School of Earth and Space Sciences, University of Science and Technology of China, Hefei 230026, China

^b State Key Laboratory of Loess and Quaternary Geology, Institute of Earth Environment, The Chinese Academy of Sciences, Xi'an, Shaanxi 710075, China

ARTICLE INFO

Keywords:

Sewage sludge
 MnO_x -N-biochar
 NH_4OH activation
 Peroxymonosulfate
 Acid orange 7 degradation

ABSTRACT

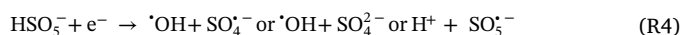
Sewage sludge (SS), the inevitable byproduct of wastewater treatment plants, is facing numerous challenges of environmentally safe and cost-effective disposal. Thus, exploration of efficient SS valorization technique is highly desired. In this study, a sludge derived carbon-supported MnO_x as a catalyst (ASMn-Nb) was synthesized through NH_4OH activation and pyrolysis (800 °C) to enhance peroxymonosulfate (PMS) decomposition and subsequent degradation of acid orange 7 and rhodamine B. The sample characterization indicated that MnCl_2 conditioning produces mixed valent Mn oxides on ASMn-Nb, while NH_4OH activation significantly enhances N-heteroatoms, surface area, and microporosity. The as-synthesized hybrid catalyst exhibited excellent PMS decomposition ability in a wide range of pH, which enhances AO7 removal efficiency 16%–100% in 40 min compared with that treated with raw sludge biochar. Moreover, the catalyst is recyclable, chemically stable, and produce negligible metal leaching during catalysis. Further investigation of catalytic mechanisms revealed that both radicle and non-radicle processes governing PMS decomposition, whereas mediated electron transfer as the primary and $^1\text{O}_2$, $\text{SO}_4^{\cdot-}$, and $^{\cdot}\text{OH}$ radicals induced catalysis as the secondary mechanisms of PMS activation and subsequent AO7 degradation. Finally, a probable mechanism of PMS decomposition over ASMn-Nb and AO7 degradation path is proposed. This study concurrently provides a facile route of improving the catalytic performance of sludge derived-biochar and a probable SS valorization technique.

1. Introduction

Advanced oxidation processes (AOPs) are effective tools for the complete decomposition of target organic pollutants in wastewater [1]. Recently, the sulfate radicle ($\text{SO}_4^{\cdot-}$) resulting from the activation of persulfate (PS) or peroxymonosulfate (PMS) shows great promise to the AOPs [2]. Compared to the $^{\cdot}\text{OH}$ radicals produced in the Fenton or Fenton-like reaction system, the $\text{SO}_4^{\cdot-}$ has strong oxidizing potentiality ($E^0 = 2.5\text{--}3.1\text{ V}$), longer lifespan (half-period = 4 s), and ability to produce in a wide pH range [3,4]. Furthermore, the $\text{SO}_4^{\cdot-}$ exhibits high degradation capacity of recalcitrant organic pollutants, environmentally friendliness, sustainability, and cost-efficiency [5]. Beside $\text{SO}_4^{\cdot-}$, PMS or PS activation also produce singlet oxygen ($^1\text{O}_2$) and superoxide ($\text{O}_2^{\cdot-}$), which showed excellent performance in organic pollutants degradation [6–8].

Up to now, several methods have been employed for activating PS or PMS such as energy input (heat, UV light irradiation, ultrasound, and

microwaves) and single-electron transfer using transitional metals (cobalt, iron, copper, zinc, and manganese) [2,9]. The energy input can break down the O – O bond to form sulfate radicals as R1 and R2 [10]. Conversely, PS or PMS can undergo a redox reaction with electron donor or activated via single-electron transfer from transitional metal for producing a sulfate radicle as R3 and R4 [1,9,10].



Although transitional metal oxides efficiently decompose PMS or PS, the significant metal leaching and requirement of a high dose of oxidants hinders the practical application of this technology [11,12]. In light of this challenge, carbonaceous materials have received significant

* Corresponding author at: CAS Key Laboratory of Crust-Mantle Materials and the Environments, School of Earth and Space Sciences, University of Science and Technology of China, Hefei 230026, China.

E-mail address: lgj@ustc.edu.cn (G. Liu).

<https://doi.org/10.1016/j.apcatb.2019.117765>

Received 23 January 2019; Received in revised form 22 April 2019; Accepted 20 May 2019

Available online 22 May 2019

0926-3373/ © 2019 Elsevier B.V. All rights reserved.

attention. PMS or PS activation process using carbocatalysts is different from the activation process of homogenous catalysis. In the PMS/Carbocatalyst system, PMS primarily activated via a non-radical path inspired by the mechanism of mediated electron transfer. Yun et al. [13,14] reported that PMS can act as an electron acceptor during oxidative degradation of organic pollutants in the presence of CNT, where the sp² carbon serves as an electron shuttling media between the organic pollutant (donor) and PMS (acceptor). The doping of heteroatoms such as N and B enhance the electron shuttling capacity of carbocatalyst [7]. In a recent study by the Yun et al. [15], low-temperature NH₃ treated nanodiamond shows a significant enhancement of PMS activation capacity due to the improvement of electron transfer efficiency. Another advantage of N-carbons is their ability to catalyzed PS even in the acidic and neutral condition [16]. On the other hand, various researchers also integrated transitional metals with the carbon template to produce metal-organic framework (MOF) and reported that the carbon template efficiently stabilized metals and enhance the composites PMS and PS activation capacity [4,17,18]. In the heterogeneous metal-based catalysts, the catalytic performance significantly depends on the nature of metal, valence state, crystallinity, structure, and surface morphology [19]. To date, transitional metals such as Fe, Co, or Mn considered as the most effective activators of PMS and PS for producing SO₄^{•-}, [•]OH, and O₂^{•-} [20]. Ahn et al. [21] reported that Co is superior to Mn, Mo, Ni, Cu, and W for producing highly reactive SO₄^{•-} from PMS activation. Besides Co, various nanostructured Mn-oxides and carbon-doped Mn also shows satisfying PMS activation capacity [22–24]. Mn oxides such as MnO, Mn₃O₄, Mn₂O₃, and MnO₂ are available in the soil [25]. Due to having redox cycles between 2⁺ and 4⁺ oxidation states, Mn oxides allow oxygen mobility in the oxide lattice and provide good redox reaction of Mn²⁺/Mn³⁺ or Mn³⁺/Mn⁴⁺ [26]. Moreover, in terms of toxicity, Mn ion is considered less toxic than that of Co ion [26,27]. Thus, Mn oxides can be a promising alternative of Co in PMS activation. Although a considerable advancement has made, the principal challenge remains in this new technology is the production of high potential activator from low-cost and available source to achieve sustainability and cost-efficiency [11].

Sludge is the inevitable byproducts of the wastewater treatment plant, which generating rapidly. The safe disposal of sludge has been a great challenge due to expensive treatment and the limitation of conventional disposal methods. Thus, researchers are looking for an efficient sludge valorization technique. A recent technology, sludge conversion into sludge derived-biochar (Sb) as an environmental catalyst, could be an alternative for safe sludge disposal and pollution remediation [28]. In recent year, adequate research has been reported about the catalytic competency of Sb in the degradation of organic pollutants by Fenton, ozonation, and photocatalytic reaction. However, a small number of studies has been focused on their PS and PMS activation potentiality [11,29,30].

Sludge contains various transitional metals/ metalloids (Fe, Al, Ca, Mg, and Si) and non-metals (C, N, S, and O). However, the contents of the sludge are different from industries to industries or different times sludge of the same industry. Hence, physiochemical features and catalytically active sites of Sb are ambiguous [11]. The simple pyrolysis of raw sludge produces Sb with low surface area and catalytically active sites. The active sites of Sb were primarily organic moieties and iron species such as Fe₃O₄ and Fe⁰. As a result of low surface area and conventional catalytically active sites, simple Sb is not always suitable for the efficient catalytic application. Therefore, various physicochemical modification or integrating organic-inorganic alloy are required to improve the surface properties and activated new catalytically active sites.

Our previous studies and literature indicate that integrating new transitional metals activate new catalytically active sites while adding natural polysaccharides improve carbon contents, surface area, porosity, and metal leaching propensity of hybrid Sb [31–35]. The surface area of Sb also can be improved by chemical activation using KOH or

ZnCl₂ [36]. Previously, various sludge derived-Fenton catalyst synthesized following those techniques. Thus, it can be hypothesized that the hybrid Sb resulting from the integration of organic-inorganic alloy and chemical activation may also exhibit higher catalytic performance for PMS activation. To the best of our knowledge, the production of hybrid Sb from the integration of sewage sludge and organic-inorganic alloy and NH₄OH activation for the subsequent decomposition of PMS and PS has not been studied yet.

Thus, the aim of this study is to evaluate the PMS decomposition potentiality of hybrid Sb, which was synthesized through single-step pyrolysis of agar-MnCl₂ integrated and NH₄OH treated sludge precursor. The effects of organic-inorganic integration and chemical activation were investigated. Then, as-synthesized hybrid Sb catalysts were characterized systematically and employed for PMS decomposition with acid orange 7 (AO7) and rhodamine B (RB) as representative pollutants. These dyes were selected due to their degradability in both PMS activated radical [12,37] and non-radical process [38]. A series of catalytic tests have been conducted to identify the main reactive species and catalytically active sites. Based on the results, a simple mechanism of PMS decomposition and subsequent degradation and mineralization of dye were proposed.

2. Methodology

2.1. Materials

Rhodamine B (C₂₈H₃₁ClN₂O₃), MnCl₂, Agar powder (C₁₂H₁₈O₉)_n, NH₄OH (28%), Potassium iodide (99.5%), KH₂PO₄, K₂HPO₄, CoCl₂, MnO, Mn₂O₃, MnO₂, Sodium bicarbonate (99.7%), *p*-Benzoquinone (BQ), Tert-Butanol, ethanol, HCl, NaOH obtained from sinopharm chemical reagent Co. Ltd, China. Acid orange 7 (C₁₆H₁₁N₂NaO₄S) (≥ 98%), Peroxymonosulfate (OXONE; KHSO₅• 0.5 KHSO₄• 0.5 K₂SO₄), potassium persulfate (K₂S₂O₈), sodium persulfate (Na₂S₂O₈), Sodium azide (NaN₃), Deuterium oxide (D₂O), Rose bengal (RB), 5, 5-Dimethyl-1-pyrroline N-oxide (DMPO), 2,2,6,6-tetramethyl-4-piperidone (TEMP) were purchased from Sigma-Aldrich. Superoxide dismutase (SOD) purchased from Aladdin Company (China). All chemicals and reagents used in this study were analytical grade and Milli-Q 18.2 MΩ cm water employed for experimental solution preparation.

2.2. Preparation of catalysts

Dewatered sewage sludge, collected from Wang Tang wastewater treatment plant, China, was first dried at 105 °C, grained, and sieved through 200 mesh size for further use. Single-step thermal decomposition of SS-laden agar-MnCl₂ alloy as a precursor used for the preparation of the catalyst. In a typical synthesis method, sludge (1 g), agar powder (1 g), and MnCl₂ (1 g) weight ratio 1:1:1 mixed with 20 ml of Milli-Q water by mechanical stirring for 1 h. Then, 7 ml of NH₄OH pour into that solution and continue stirring for a further 3 h. The resulting solution was then dried in an oven at 65 °C overnight for chemical reaction and afford dark yellow solid. Then, that dried solid was placed in a muffle furnace for thermal treatment at 800 °C for 1 h (10 °C/ min. of heating rate) under Ar atmosphere. The resulting biochar was then crushed and sieved through 200 mesh size, rinse several times with ethanol and Milli-Q water, and labeled as ASMn-Nb. The reference samples such as raw sludge (Sb), sludge-agar (ASb), and sludge-agar-MnCl₂ (ASMnb) biochar without NH₄OH treatment were also prepared following the same synthesis route for comparison.

2.3. Characterization

The physicochemical properties of catalysts were characterized as follows: the surface morphology was observed by SEM images equipped with X-ray energy dispersive spectrometer (EDS, Sirion 200, FEI Electron Optics Co., USA). Surface textural properties were analyzed by

Brunauer–Emmett–Teller (BET) and Barrett–Joyner–Halenda (BJH) method (Tristar II 3020 Micromeritics). The percentage of major elements were determined by X-ray fluorescence (XRF) with X-ray spectrometer (ZSX Primus II, Japan). Thermal stability and char-inorganic contents quantification were analyzed by Thermogravimetric analysis (TGA, Q5000 V3.17 Build 265). Crystalline phase structure was detected by X-ray diffraction peaks (XRD, Rigaku D/max 2400). Surface chemical compositions were analyzed by X-ray photoelectron spectroscopy (XPS, ESCALAB 250xi, ThermoFisher Scientific) and Fourier transform infrared (FTIR, Thermo Nicolet-8700) analysis. The reactive oxygen species (ROS) were detected by electron spin resonance (ESR) techniques (JES-FA200, JEOL Co., Japan). The detail parameters of characterization techniques reported elsewhere [39].

2.4. Catalytic activity test

The catalytic performance of the as-synthesized catalysts towards PMS activation was evaluated by the degradation of AO7 and RB. The effects of contact time, ambient pH, and PMS dose has been investigated. The catalyst was recycled five times to identify material stability, metals leaching propensity, and economic feasibility. In a typical procedure, 20 mg catalyst added into 100 ml dye solution (20 mg L^{-1}) in a 250 ml glass beaker. Then, the mixture placed in a mechanical shaker at 180 rpm for 1 h to achieve adsorption-desorption equilibrium. Afterward, the residue catalyst collected by filtration and employed in catalytic reaction with 100 ml dye (20 mg L^{-1}) and PMS (1.64 mM) mixture solution. To investigate pH effects, the initial pH of the solution adjusted to the desired value by using concentrated HCl and NaOH solution, and 1 mM phosphate and carbonate buffers added to maintain the neutral and alkaline pH, respectively. Besides PMS, the oxidation potentiality of Potassium persulfate (KPS) and Sodium persulfate (SPS) also investigated. To evaluate the dye concentration during reactions 1 ml solution were withdrawn and added with 0.1 ml of $\text{Na}_2\text{S}_2\text{O}_3$ solution (100 mM), filtrated through NY $0.45 \mu\text{m}$ syringe filter, and measured immediately by an UV–vis spectrophotometer (2450). The UV–vis spectrophotometric absorbance 486 nm and 554 nm used for AO7 and RB concentration measurement, respectively. The metal contents in solution after catalysis were measured by ICP-AES analysis. Furthermore, the effects of biochar dose on PMS decomposition in the absence of dye also measured by modified iodometric titration method [40]. The responsible ROS for PMS decomposition were identified by scavenging experiments and Electron spin resonance (ESR) techniques with adding DMPO, SOD, and TEMP. The degradation and mineralization of dyes were confirmed by the degraded product analysis using LC–MS analysis.

3. Results and discussion

3.1. Characterization of catalysts

The surface morphology of the as-synthesized catalysts was observed by SEM images. As shown in Fig. 1, sludge biochar (Sb) shows a ragged and irregular surface with some porous feature. When SS integrated with Mn and agar, resulting biochar composites shows agglomeration of Mn and sludge over the agar surface, where ASMn-Nb shows more porosity and cracked surface with irregular nanoparticles dispersion. Transitional metals (Fe, Al, Ca, Mg, K, and Mn), metalloids (Si), and nonmetals (C, P, and O) were detected on the samples by EDS analysis (Fig. S1).

The general physiochemical properties of composites listed in Table 1. The BET and pore analysis shows that the surface area and porosity of composites were entirely different. Due to the rugged surface feature, sludge biochar (Sb) shows a surface area about $42 \text{ m}^2 \text{ g}^{-1}$. After integrating sludge with agar the surface area of ASb increase to $66 \text{ m}^2 \text{ g}^{-1}$, which could be due to the dispersion of SS over the surface of agar. However, the surface area decreases in ASMn by Mn

integration, indicating the formation of metal oxides which leads to penetrate nanostructured metals and obstruct the formation of microspore. Thus, the average pore diameter increases in ASMn. The surface area and porosity significantly improve by pretreating the complexes with NH_4OH . As shown in Table 1 and Fig. 2a, ASMn-Nb has the higher BET surface area of $157 \text{ m}^2 \text{ g}^{-1}$ and height total pore volume of $0.136 \text{ cm}^3 \text{ g}^{-1}$, which was much higher than the non- NH_4OH treated ASMn and other sludge biochar composites. Moreover, the average pore diameter of ASMn-Nb is smaller than that of other samples, which could be due to the function of NH_3 -derived etching radicals (H , NH , and NH_2) during NH_4OH activation and pyrolysis process [41]. The BJH pore size distribution of catalysts measured by the desorption branch (Fig. 2b), it shows that the pore size distribution of ASMn-Nb is higher in the lower pore diameter zone. According to the IUPAC classification, the N_2 adsorption-desorption isotherm curve shown by sludge composites are type IV feature with H4 hysteresis pattern, indicating narrow slit-like pore structures (Fig. 2a) [42]. The elemental ratio in catalysts was measured by XRF analysis. The result indicates that catalysts have complex constituents, where the primary components are C, SiO_2 , Al_2O_3 , Fe_2O_3 , MnO, P_2O_5 and some CaO, MgO, K_2O , Na_2O , SO_3 , CuO, TiO_2 , Cr_2O_3 , ZrO_2 , and ZnO (Table 1). Integrating agar and Mn increased C and MnO_x contents in the catalysts, respectively, where other metal oxides were reduced.

The TGA and DTGA plot of the biochar composites displayed in Fig. 2c. As shown, Sb exhibits two weight loss region at 40°C and 450°C indicating loss of moisture and oxidation of char. The initial and final decomposition temperature and weight loss ratio were changed by integrating agar and MnCl_2 . For ASb, the decomposition temperature increased to 490 and 540°C indicating decomposition of more char contents. However, decomposition temperature reduces after Mn integration, which should be due to the formation of metal oxides [43]. In both ASMn and ASMn-Nb, the weight loss region observed at ~ 415 and $\sim 500^\circ\text{C}$ indicating the decomposition of oxygen functional groups and char contents, respectively [31], where the char contents in ASMn-Nb is comparatively higher than ASMn based on the DTGA intensity at 500°C . No weight losses observed in the samples after 600°C confirms no secondary decomposition or losses of active products. The TGA curve also evaluated the quantitative loading of inorganic metals on samples by weighing the residue [43–45]. The inorganic contents in Sb, ASb, ASMn, and ASMn-Nb were calculated as 75.69, 61.88, 67.23, and 66.64%, respectively. The crystalline phase structures of samples were investigated by XRD diffraction peaks. Fig. 2d shows that quartz SiO_2 are present in all sludge composites (please see Table S1 for XRD peaks 2θ and corresponding hkl value), where both ASMn and ASMn-Nb shows new peaks for spessartine-syn, MnO_2 , and Sekaninaite, which was due to the polymerization of Mn and sludge components. The Raman spectra of samples show two main peaks at 1360 cm^{-1} (D band) and 1608 cm^{-1} (G band) corresponding to the defects and distortion of carbon atomic crystals and plane stretching motion between sp^2 carbon atoms, respectively (Fig. 2e) [46,47]. The integrated intensity ratio of D band and G band (I_D/I_G) clearly indicates the degree of defects in carbon materials. Thus, the higher I_D/I_G value of ASMn-Nb (0.929) and ASMn (0.912) than ASb (0.893) indicates higher defected carbon, which can be attributed to the reduction of oxygen functional groups and the introduction of heteroatoms by Mn integration and NH_4OH treatment, respectively [46,48]. A hunch observed in ASMn-Nb at 650 cm^{-1} , indicates the asymmetric stretching of metal and hydroxide group [46].

The surface chemical composition of catalysts was investigated by XPS and FT-IR analysis. The wide XPS spectrum shows that catalysts are primarily composed of C, O, N, and some Al and Si (Fig. S2). The Mn 2p peaks only observed in ASMn and ASMn-Nb. For detail investigation of the chemical composition, we deconvoluted high-resolution XPS peaks of catalysts (Fig. S3), and the summary of XPS atomic distribution was presented in Fig. 3a. It shows that the C atom ratio in catalysts significantly increases by agar and Mn inclusion, which is

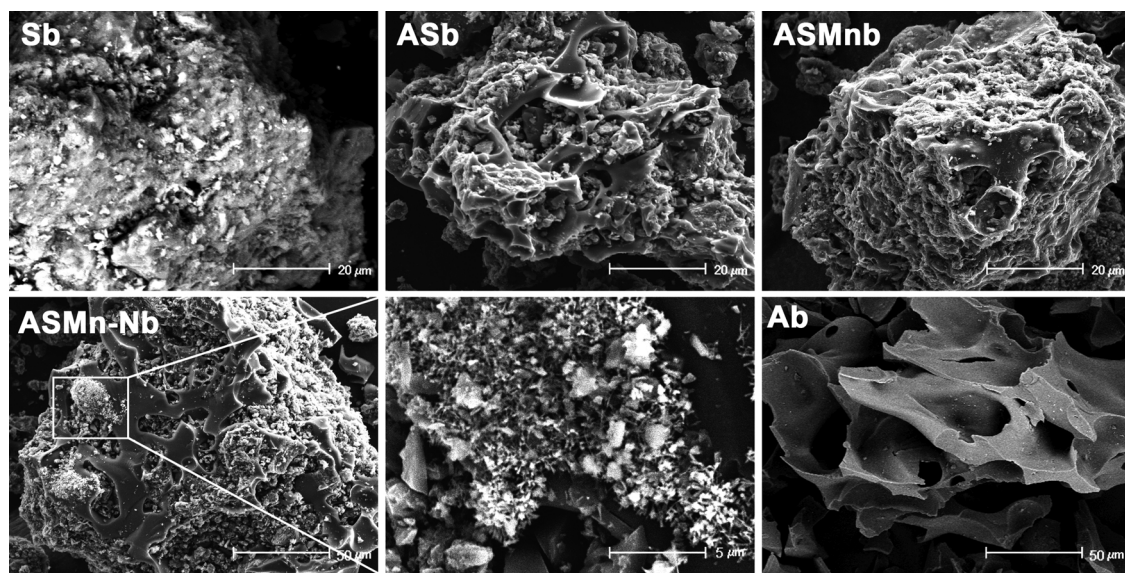


Fig. 1. SEM images of as-synthesized catalysts; Sludge biochar (Sb), Sludge/ Agar biochar (ASb), Sludge/ Agar/ MnCl_2 biochar (ASMnb), Sludge/ Agar/ MnCl_2 biochar pretreated with NH_4OH (ASMn-Nb), and Agar biochar (Ab).

Table 1
Surface textural properties and oxides groups of catalysts.

	Sb	ASb	ASMnb	ASMn-Nb	Ab
S_{BET} ($\text{m}^2 \text{g}^{-1}$)	42	66	50	157	482
D_{avg} (nm)	8.50	5.46	7.77	3.58	27.08
V_{total} ($\text{cm}^3 \text{g}^{-1}$)	0.090	0.059	0.096	0.136	0.060
Contents percentage (%)					
C	17.16	28.07	52.26	39.04	90.84
SiO_2	49.27	46.64	24.76	31.04	
Al_2O_3	14.15	11.37	5.41	7.45	
Fe_2O_3	4.67	3.18	1.63	2.32	
MnO	0.06	0.07	7.07	10.21	
P_2O_5	4.05	2.92	0.87	1.59	
SO_3	0.89	0.98	0.91	1.23	
CaO	2.37	1.81	0.72	1.23	
MgO	1.64	1.24	0.65	0.82	
K_2O	2.19	1.69	0.16	0.19	
Na_2O	2.37	0.80	0.17	0.45	
CuO	0.06	0.04	0.04	0.04	
TiO_2	0.98	0.75	0.37	0.55	
Cr_2O_3	0.05	0.05	0.04	0.04	
ZrO_2	0.03	0.02	0.02	0.02	
ZnO	0.06	0.03	0.03	0.03	

corresponding to the high C contents in agar biochar and the reduction of surface oxygen due to polymerization with Mn. The C 1s XPS peak of catalysts can be deconvoluted into 4 gaussian peaks at 284.69, 285.71, 286.91, and 289.28 eV for C–C/ C=C, C–O/ C–N, C=O, and COOH, respectively (Figs. 3b and S3). Based on the deconvoluted peak area calculation (Table S2), both ASMn-Nb and ASMnb have higher C–C/ C=C and COOH atomic ratio than ASb and Sb. The O 1s high-resolution peak can be deconvoluted into six peaks (Fig. 3c). Peaks at 529.78 and 530.58 eV attributed to lattice oxygen of Mn–O and Al–O [29]. The new peak appears at 531.36 eV after integrating Mn could be ascribed to some oxygen defects in the mixed metal crystal of Mn, Al, Fe, and Si (Fig. S3). Other peaks at 532.51, 533.61, and 534.57 eV attributes to Si–O of sheet-type silicate, C–O, and COOH, respectively [29,49]. Since the total oxygen atomic ratio reduced significantly after Mn integration (Fig. 3a), the defects oxygen assumed to be produced near 531.36 eV by losing oxygen from the crystal as a result of polymerization. Fig. 3d displayed the N 1s peak deconvolution for pyridinic N, pyrrolic N, graphitic N, and oxidized N at 398.38, 399.89, 400.96, and 401.86 eV. The N content of ASMn-Nb (3.9%) increase significantly than that of

ASMnb (1.6%) and other catalysts, implying that NH_4OH activation of sludge precursor able to anchor more N atom in the composite (Table S2). It has been widely reported that the involvement of Pyridinic N and graphitic N of carbonaceous materials are suitable to enhance electrochemical performance [50,51]. They can lead to electron withdrawing from adjacent carbon and non-uniform distribution which improve the catalytic activity of material [52]. The Mn high-resolution spectra give to major peaks for Mn 2p_{3/2} and Mn 2p_{1/2} (Fig. 3e). The Mn 2p_{3/2} major peak deconvoluted into three peaks at 641.12, 642.60, and 644.49 eV, which can be attributed to oxidized Mn species of MnO [53], Mn_2O_3 [54], and MnO_2 [55–57], respectively. The Mn 2p_{1/2} core level region shows two peaks at 653.33 and 654.61 eV corresponding to the Mn^{3+} [54] and Mn^{4+} [58], respectively. It shows that the mixed-valent Mn present in the catalyst, while the ratio of Mn^{2+} , Mn^{3+} , and Mn^{4+} in ASMn-Nb is 1: 1.8: 1.3. The Fe 2p peaks show that the Fe^{2+} and Fe^{3+} valent iron existed in the catalyst (Fig. 3f). Further, the surface functional groups of catalysts were measured by FT-IR analysis (Fig. 2f), which support the results of XPS. The characteristics FT-IR peaks and assignment listed in Table S3.

3.2. Catalytic performance of the catalyst

A series of experiments were conducted to evaluate the PMS decomposition ability of catalysts. Before catalytic reaction, catalysts were treated with pollutants for adsorption-desorption equilibrium. Fig. S4a and b shows that catalyst ASMn-Nb exhibits superior AO7 and RB adsorption capacity than other as-synthesized catalysts, owing to the high surface area and pore structure as shown in BET results, and the adsorption-desorption equilibrium of entire catalysts achieved within 40 min. The high sorption capacity of the catalyst may be favorable for high mass transfer of reactants. Fig. 4a displayed the AO7 degradation performance of catalysts in the PMS system. A control test using AO7 and PMS shows only 4.1% AO7 reduction after 1 h, indicating PMS itself has a negligible contribution to AO7 degradation. Using ASMn-Nb, the removal capacity of AO7 is 91.4% after 20 min and 100% after 40 min, which is the greater AO7 reduction ability comparing other as-synthesized catalysts. The degradation kinetics of AO7 can be fitted by the pseudo-first-order equation, where the reaction rate constants were measured by Eq 1.

$$\ln(C_t/C_0) = -K_{\text{cat}}t \quad (1)$$

Where, C_0 and C_t is the pollutant concentration at initial and t time

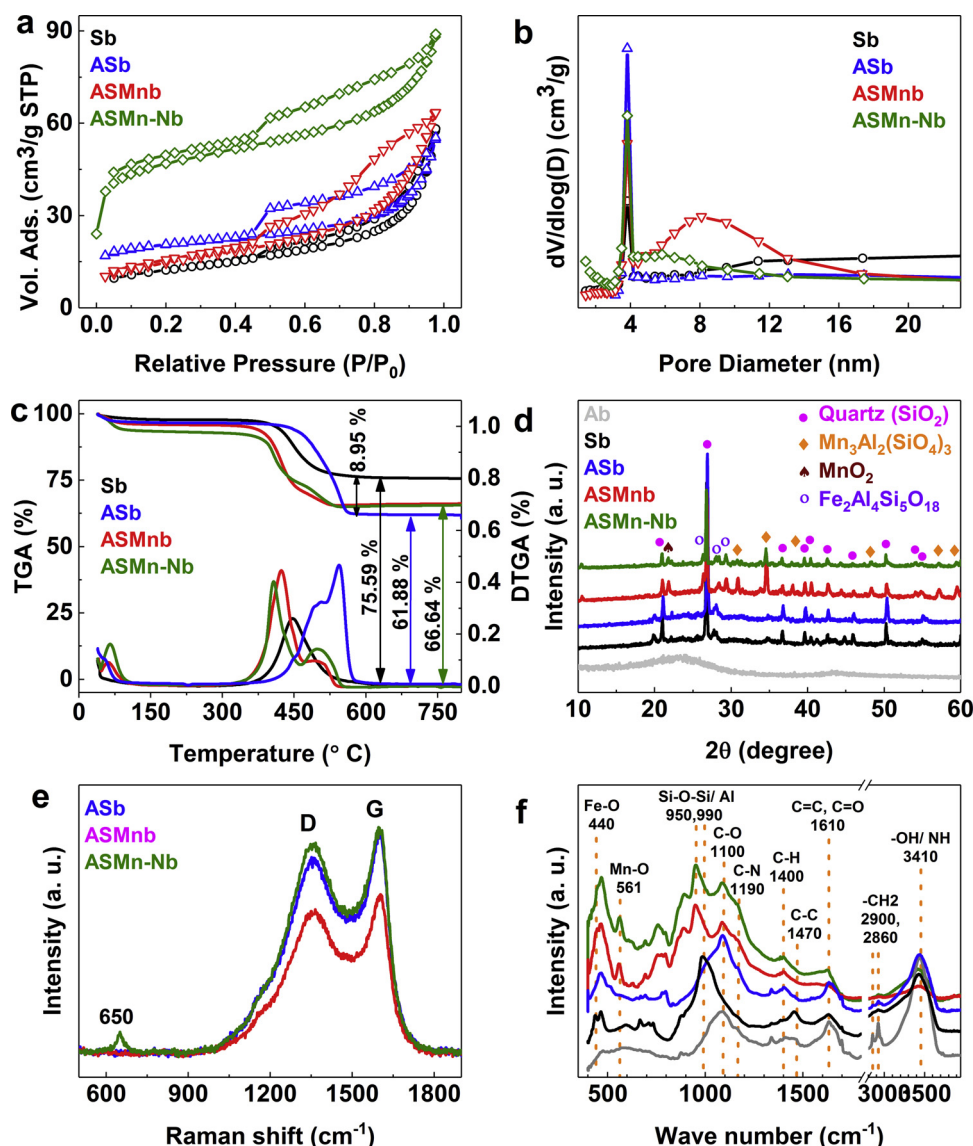


Fig. 2. BET (a), pore (b), TGA and DTGA (c), XRD (d), Raman (e), and FT-IR (naming of samples similar to XRD) (f) characterization of catalysts.

interval, t is the reaction time, and K_{catal} is the reaction rate constant.

Fig. S4c displayed the linear relationship of $-\ln(C/C_0)$ versus time plot for AO7 degradation over as-synthesized catalysts in the PMS system. Most rapid degradation of AO7 occurred in the presence of ASMn-Nb. The reaction rate constant of ASMn-Nb ($K_{ASMn-Nb} = 0.106 \text{ min}^{-1}$) is significantly higher than ASMnb ($K_{ASMnb} = 0.059 \text{ min}^{-1}$) and other as-synthesized sludge catalysts. This phenomenon indicates that ASMn-Nb is efficient in degrading AO7. On the other hand, the reaction rate constant of Sb is 0.047 min^{-1} , and only 16% AO7 can be removed in 40 min of reaction. The Mn loading over SS- agar complex and the enhancement of N-atoms, surface area, and porosity by NH_4OH treatment may be played the key role for the superior catalytic activity. The identification of catalytically active sites and their role in PMS decomposition were discussed in the mechanisms section. Fig. 4b displayed the UV-vis spectra of AO7 at initial and different time intervals of degradation by ASMn-Nb. The main adsorption band can be seen at 486 nm which reflects the concentration of AO7 in the solution. It shows that the intensity of adsorption band at 486 reduces 79.2%, 91.4%, and 100% at 10, 20, and 40 min of reaction. However, rapid removal of AO7 can be observed in simultaneous adsorption and catalytic reaction system, where 100% AO7 removal achieved within 10 min (Fig. S4d).

It is well known that solution pH plays a crucial role in PMS decomposition [10]. Thus, the impact of solution pH on the catalytic reaction also investigated. Fig. 4c shows that AO7 degradation efficiency is nearly similar in pH range from 2 to 10, indicating ASMn-Nb is efficient for catalytic reaction in a wide range of pH. However, a slight rapid degradation at pH 6 to 10, and the reduction of degradation efficiency at pH 12 was observed. The control test for AO7 degradation by PMS without adding ASMn-Nb in different pH also conducted. The dot lines in Fig. 4c shows that AO7 almost unchanged at pH from 2 to 8. However, rapid degradation at pH 10 and 12 observed, which is due to the self-decomposition of PMS at the pH above pK_a value (9.3) [59]. At pH 12, AO7 degradation by PMS self-decomposition decreases, which could be due to the involvement of a high concentration of OH^- in competing reactions with generated reactive species. The AO7 degradation by PMS self-decomposition in terms of pH is consistent with Qi et al. [60] study.

PMS concentration is another important factor for influencing catalytic reactions. Usually, a high dose of PMS may increase the reaction rate. However, the high concentration of SO_4^{2-} ion is not welcome to the water system due to its corrosive characteristics [11]. Thus, minimal PMS for the optimum catalytic reaction is suitable for environmental and cost perspectives. In this study, a rapid reduction of

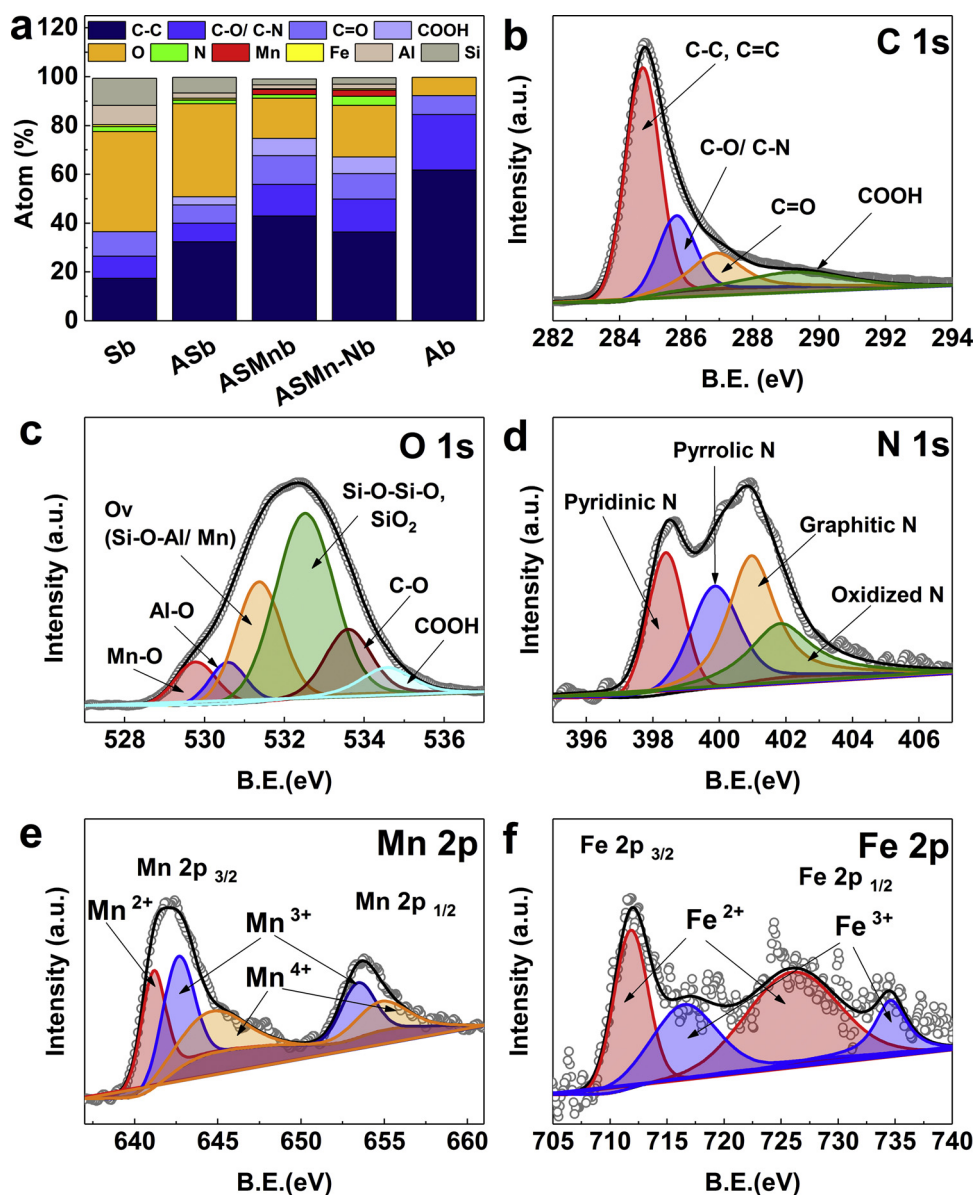


Fig. 3. Atomic distribution percentage of catalysts (a) and High-resolution C 1s (b), O 1s (c), N 1s (d), Mn 2p (e), and Fe 2p (f) XPS peaks of ASMn-Nb.

AO7 can be observed while the PMS/ AO7 ratio is high (Fig. S5a). The $-\ln(C/C_0)$ versus time plot for AO7 removal in different PMS dose illustrated in Fig. 4d, it shows that the slope is significantly increased with the rising PMS concentration, indicating the enhancement of reaction rate (Table S4). Thus, the reaction rate constant of AO7 shows a significant correlation with the PMS/ AO7 ratio (Fig. 4d inset). From this measurement, it was estimated that for a 1 h catalytic reaction, minimal PMS/ AO7 ratio above 3.1 is required for complete removal of AO7 (20 mg L^{-1}) by using 0.2 g L^{-1} of ASMn-Nb (Fig. S5b). Besides PMS, Potassium persulfate (KPS) and Sodium persulfate (NPS) activation potentiality of ASMn-Nb also investigated. Fig. S5c shows that AO7 degradation achieved 99.9% and 93.2% after 120 min reaction using 1.6 mM of KPS and NPS, where complete reduction of AO7 achieved within 40 min using a similar dose of PMS, indicates lower oxidation effectiveness of KPS and NPS.

In the case of RB, the degradation rate reduced than that of AO7. Fig. S5d displayed the removal rate of RB by using ASMn-Nb. The reaction rate constant of RB degradation (0.086 min^{-1}) is lower than that of AO7 degradation. The UV-vis adsorption spectra at 554 represent the RB concentration during degradation (Fig. S5e), it clearly shows that

after 60 min reaction adsorption band at 554 nm reduces almost 99.7%, indicating ASMn-Nb also efficient in degrading RB. Based on the performance of catalysts, a brief comparison of ASMn-Nb and some previously reported catalysts were presented in Table S5. As listed, the ASMn-Nb shows excellent catalytic performance in dye degradation considering the PMS/ dye ratio, catalyst concentration, and reaction kinetics.

The effects of catalyst dose on the decomposition of PMS further investigated by modified iodometric titration method [11,40], where the yellow color of initial and t times treated PMS solution obtained by proper mixing with KI and NaHCO_3 in a ratio of PMS: KI: $\text{NaHCO}_3 = 0.5 \text{ mM}: 60 \text{ mM}: 70 \text{ mM}$, and the concentration were detected by UV vis spectrophotometer at 352 nm. Fig. 5a shows that the $-\ln(C/C_0)$ versus time slope significantly increase with the dose of ASMn-Nb. The reaction rate constant almost proportionally increases with the catalyst dose, indicating increasing PMS decomposition and/or sorption rate with rising catalyst concentration. The complete removal of 3.25 mM of PMS can be achieved within 40 and 60 min by using 0.8 and 0.4 g L^{-1} of ASMn-Nb, respectively (Fig. S5f). The UV-vis spectra of PMS solution in iodometric system displayed in Fig. 5b. As it shows, the

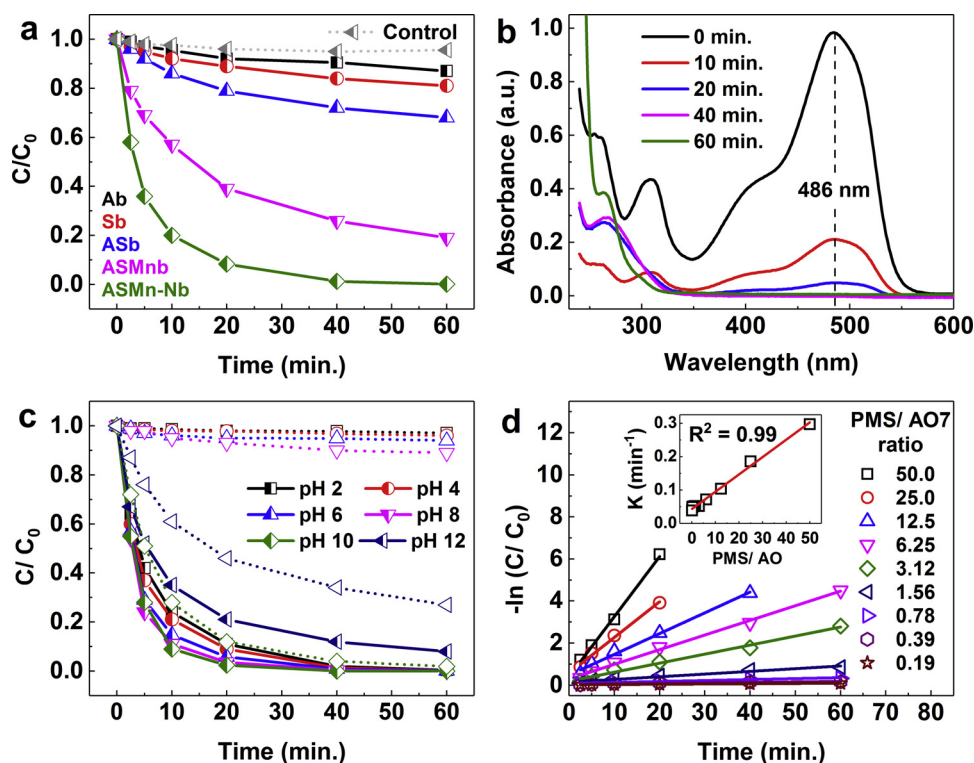


Fig. 4. AO7 removal performance by using as-synthesized catalysts in PMS system (a), Time-dependent UV-vis spectra of AO7 degradation by ASMn-Nb (b), effects of ambient pH on AO7 removal, (c) $-\ln(C/C_0)$ versus time plot for AO7 degradation in various PMS dose (d). Experimental conditions: catalysts = 0.2 g L⁻¹, AO7 = 20 mg L⁻¹, PMS = 1.6 mM, pH = 6 and 8 (1 mM phosphate buffer), 10 and 12 (1 mM bicarbonate buffer), T = 25 °C.

UV-vis adsorption spectra at 352 nm completely disappear after 1 h for 0.4 and 0.8 g L⁻¹ of ASMn-Nb, thus, no yellow color obtained after mixing with KI and NaHCO₃ (Fig. 5b inset).

The chemical stability and the recyclability of the catalyst are of great importance to evaluate the economic feasibility and propensity of secondary pollution. For recycling tests, the spent biochar was collected by centrifugation and filtration, rinsed with Milli-Q water several times

and dried at 80 °C for further use. Fig. 5c shows that after 5 times recycling, AO7 degradation potentiality is almost similar. Although a slight reduction in degradation rate can be observed, the complete degradation of AO7 still can be achieved by extending reaction time. Furthermore, ASMn-Nb also employed for the high concentration of PMS/AO7 system (Fig. S6a). However, the degradation efficiency is not as satisfactory as the low concentration solution. By recycling ASMn-Nb

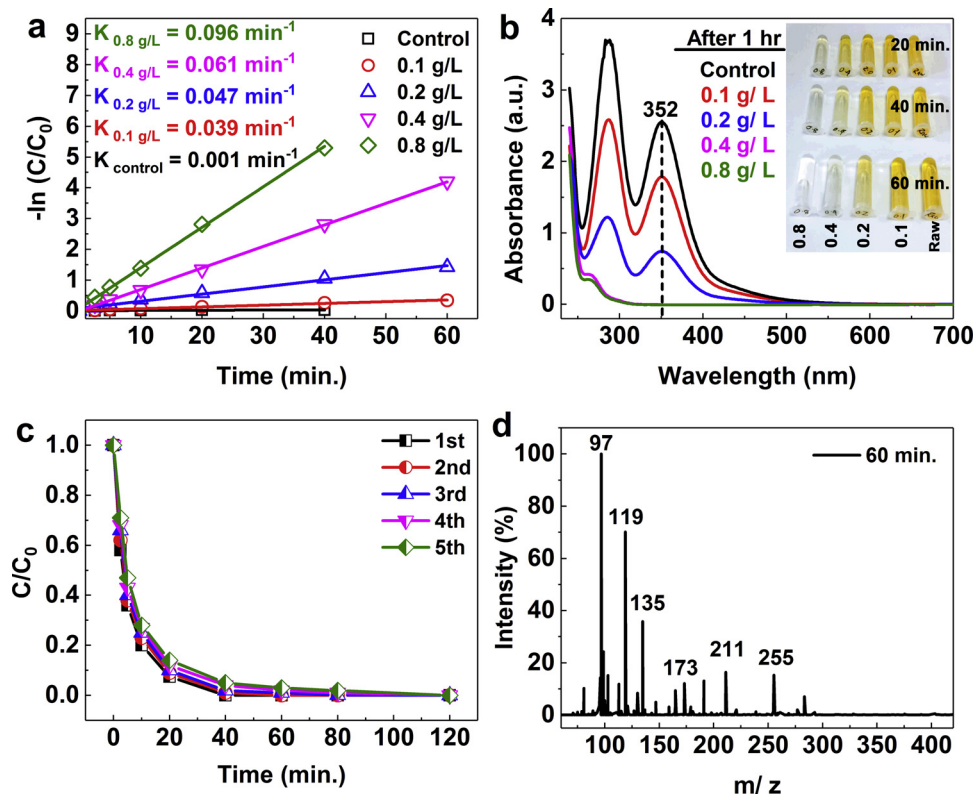


Fig. 5. $-\ln(C/C_0)$ versus time plot for PMS decomposition by different dose of ASMn-Nb (a), UV-vis spectra of PMS in iodometric measurement system after 1 h treated with ASMn-Nb (b), recyclability of ASMn-Nb for AO7 removal (c), ESI-MS analysis of the intermediates formed in AO7 degradation. Experimental conditions for (a) and (b): PMS = 3.25 mM, prepared solution for UV-vis spectra; PMS (0.5 mM) + KI (60 mM) + NaHCO₃ (70 mM); for (c) and (d): catalyst = 0.2 g L⁻¹, AO7 = 20 mg L⁻¹, PMS = 1.6 mM; pH = 6 (1 mM phosphate buffer), T = 25 °C.

(50 mg L⁻¹) 4 times in the 100 mg L⁻¹ of AO7 and 3.2 mM PMS system, the degradation capacity reduced from 98.4% to 54.8%, which is due to the blockage of some active sites by sorption and losses of biochar during recovery. The metal leaching propensity after the catalytic reaction was measured by ICP analysis (Table S6). The Fe leaching cannot be detected while the Mn leaching propensity is very negligible, indicating good chemical stability of the catalyst. Although the metal leaching is negligible, further experiments were conducted to evaluate the contribution of leached trace metals ion on the activation of PMS and subsequent degradation of AO7. The supernatants of ASMn-Nb and ASMn-Nb/ PMS system were collected by filtration after 1 h reactions and then fresh AO7 was introduced into the system to measure the leachate contribution in catalysis. Fig. S6b and c shows that there are no changes of AO7 concentration at pH 6 to 8, while about 6.5% and 4.2% reduction of AO7 observed for supernatants of pH 2 and pH 4 of ASMn-Nb/PMS system. This result evident that the contribution of homogenous catalysis by leachate metal ions was negligible. Furthermore, the XRD and XPS spectrum of fresh and spent catalyst displayed in Fig. S7a and b. Compared to the fresh sample, no considerable changes in the XRD and SPX profile of the recycled sample observed, which indicating metal stability. The catalytic performance of ASMn-Nb also compared with the pure Mn oxides. Fig. S6d shows that ASMn-Nb outperforms Mn²⁺, Mn³⁺, and Mn⁴⁺. The sorption capacity of Mn ions was negligible. After 40 min of catalytic reaction, AO7 removal capacity of ASMn-Nb, Mn³⁺, Mn⁴⁺, and Mn²⁺ was 100, 79, 39, and 8%, respectively.

The intermediates formed in the AO7, PMS, and ASMn-Nb system were identified by ESI-MS negative iron analysis. Fig. S8 shows that molecular AO7 before catalytic reaction gives an intense peak at 327 *m/z*. After 60 min reaction, peaks at 327 completely disappear, indicating complete destruction of molecular AO7 (Fig. 5d). An intense peak appears at 97 *m/z* attributed to the HSO₄⁻. The breakdown of AO7 molecular structure can be suggested by peaks at 119, 135, 165, 173, 191, 211, and 255 *m/z*. The intense peaks at 119 and 135 *m/z* could be ascribed to H atom abstracted tartronic acid and dihydroxymalonic acid which further mineralized to CO₂ and H₂O. Based on the above results and literature, a simple mineralization pathway of AO7 illustrated in Fig. S9.

3.3. Mechanisms of catalytic process

In order to reveal the impacts of reactive radicals in AO7 degradation, quenching experiments in the presence of various radical scavenger was conducted. Ethanol (EtOH), tert-butanol (TBA), *p*-Benzoquinone (BQ), and sodium azide (NaN₃) used as scavengers for SO₄^{•-}, [•]OH, O₂^{•-}, and ¹O₂, respectively. It also noted that [•]OH can be inhibited by both TBA and EtOH, while SO₄^{•-} tends to react with EtOH rather than TBA. In addition, NaN₃ also have some affinity to react with SO₄^{•-} and [•]OH besides ¹O₂ [7]. Fig. 6a shows that the scavenging effects of EtOH, TBA, and BQ are weaker than that of NaN₃. Employing a high dose of EtOH and TBA (PMS and scavengers molar ratio = 1:1000) results in 5.6 and 9.4% decline of degradation efficiency than that of control test (no scavengers use) in 1 h. When employed BQ at the ratio of 1:25, the degradation capacity reduced by 13.2% in 1 h. On the other hand, NaN₃ significantly dropped the removal efficiency. For PMS and NaN₃ molar ratio of only 1:1, the reduction efficiency dropped 27.3% in 1 h, which raised to 55.2% by 1:25 dose. The UV-vis spectra show that extending the reaction time for 2 h have no significant improvement of AO7 degradation in the NaN₃ quenching reaction (Fig. S10). This phenomenon indicates that singlet oxygen is the dominant reactive species followed by O₂^{•-}, [•]OH, and SO₄^{•-} for AO7 degradation. Although NaN₃ widely used as ¹O₂ quencher, Yang et al. [61] reported that PMS can be consumed by excess NaN₃ through direct reaction. Therefore, it is possible that the quenching effects shown by using NaN₃ could be due to the depleting of PMS. To explore this, the depletion of PMS and KPS by different concentrations of NaN₃ measured by

colorimetric method. Fig. 6b shows that 1.6 mM of PMS completely depleted within 5 min by using 50 mM of NaN₃, even the moderate dose of NaN₃ (1.5 mM) also contributes to reducing PMS concentration over time. To avoid this, scavenging experiment for the activation of KPS was conducted which exhibits almost no depletion by access NaN₃ (Fig. S11a). As displayed in Fig. S11b, the performance of various radical quencher in the KPS system is almost similar to the results of the PMS system. However, the activation path for asymmetric PMS and symmetric KPS could be different due to their molecular difference [19]. In the case of KPS activation, ¹O₂ can be produced by the carbonyl groups and Mn³⁺/Mn⁴⁺ redox reaction [62], while PMS usually showed more sensitivity to the polarized carbon adjacent to N atoms with greater absorptivity and carbon-based non-radical activation tendency [20,62]. To validate ¹O₂ production in the ASMn-Nb/PMS system, the H₂O solvent was exchanged with D₂O, as the lifetime of singlet oxygen extends up to 10 times in D₂O. Fig. 6c shows that solvent exchange does not exhibit any kinetic effects on AO7 degradation, which do not support the usual nature of ¹O₂ in D₂O. The effects of solvent exchange in ¹O₂ induced catalysis were confirmed by comparing AO7 degradation in Rose Bengal (RB)/light irradiation system (a benchmark of ¹O₂ producer). Fig. S11c shows that in the visible light irradiation/RB condition, AO7 degraded rapidly in the D₂O medium. The reaction rate constant in D₂O was 3.2 times higher than that of the H₂O solvent which evident the usual properties of ¹O₂ and deny singlet oxygenation in ASMn-Nb/PMS system. Furthermore, the pH effects showed that the AO7 removal efficiency in the neutral and alkaline condition is almost comparable (Fig. 4c). Since AO7 undergoes deprotonation under weak or strong alkaline condition, being transferred into more electron-rich species. Singlet oxygen as a highly selective oxidant exhibits much better reactivity toward deprotonated species, thus, alkaline condition is expected to enhance catalytic reaction rate, which was not a case in this study. Therefore, the results of pH effects also contradict the singlet oxygenation. However, TEMP-¹O₂ adducts have been recorded in the EPR study, which provides a basis of singlet oxygenation (Fig. 6d). Previous studies reported that TEMPO signals in EPR measurement could be produced by the formation of TEMP^{•+}, as a result of CNT mediated electron transfer process from TEMP to PMS, instead of ¹O₂ [13,63]. Considering the above findings, it was suggested that there are inadequate ¹O₂ produced in the PMS/ASMn-Nb system which shows no noticeable effects in solvent exchange and pH experiments. To identify O₂^{•-} radicals, EPR signals in the presence of superoxide dismutase (SOD) and PMS/ASMn-Nb recorded after 10 min of reactions. However, no peaks were detected to confirm O₂^{•-} (Fig. 6d). Therefore, the elevation observed in the UV-vis spectrum at 350–550 nm region, which determined the effects of O₂^{•-} in AO7 degradation, could be due to the formation of quinhydrone complex (BQ–HQ) produced by electron transfer from the catalyst (Fig. S10) [64]. Quenching experiments also evident that some SO₄^{•-} and [•]OH were produced. Thus, AO7 degradation in PMS/ASMn-Nb compared with the Cobalt/PMS system (a benchmark of SO₄^{•-} producer). Fig. S11d shows that AO7 rapidly degraded by Co²⁺/PMS system due to the production of highly reactive SO₄^{•-}, consequently, quenched 97.1% by using EtOH. In the case of ASMn-Nb/PMS, the reaction rate constant reduced 1.31 times by EtOH quencher, indicating the existence of SO₄^{•-}. Furthermore, the EPR spectrum shows some weak signals for DMPO-[•]OH and DMPO-SO₄^{•-} which intensity disappear over time, indicating some SO₄^{•-} and [•]OH were produced and consumed by AO7 (Fig. 6e).

Since the dominant effects of singlet oxygenation cannot be validated and the oxidative effectiveness merely impacted by other quenchers, a non-radical process governing by N-carbon should be played the primary role in AO7 degradation instead of radical induced catalysis. Duan et al. [20] reported that radical scavengers barely impacted the oxidative efficiency of a non-radical process governing by defective graphene. To identify the role of N-carbon, AO7 degradation in PMS/ASMn-Nb system compared with the AS-Nb biochar (agar and sludge combined biochar pretreated with NH₄OH without conditioning

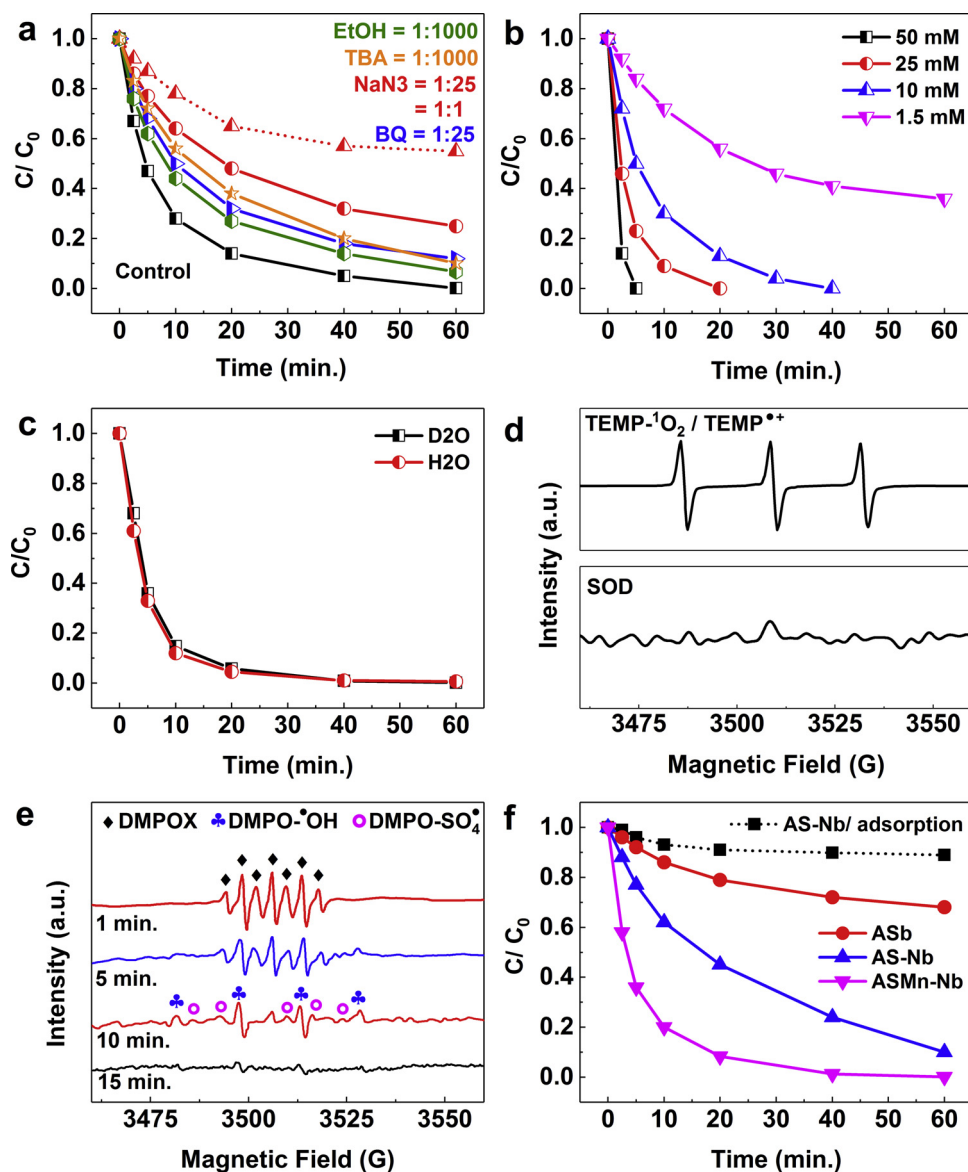


Fig. 6. Effects of scavengers on AO7 degradation in PMS + ASMn-Nb system (a), depletion of PMS by different ratio of NaN $_3$ (b), effect of solvent exchange on AO7 degradation (c), ROS identification using EPR spectra (d) and (e), and degradation of AO7 in different sludge biochar system. Experimental conditions: catalysts = 0.2 g L $^{-1}$, AO7 = 20 mg L $^{-1}$, PMS = 0.8 mM for (a) and 1.6 mM for (b), (c), and (f), pH = 6 (1 mM phosphate buffer), T = 25 °C.

MnCl $_2$). Fig. 6f shows that AS-Nb also efficiently degrade AO7, however, the reaction rate was lower than ASMn-Nb. The defective carbon corresponding to N-doping was the only factor responsible for the enhancement of catalytic performance of AS-Nb than that of non-NH $_4$ OH treated agar and sludge combined biochar ASb (see the Raman spectra in Fig. S12a). In the case of ASMn-Nb, the N-carbon along with MnO $_x$ synergistically performed non-radical (major) and radical (minor) process for the activation of PMS and subsequent degradation of AO7. Therefore, ASMn-Nb shows rapid AO7 degradation.

Based on the above findings, the mechanisms of PMS decomposition over ASMn-Nb and subsequent degradation of AO7 illustrated in Fig. 7. Due to the presence of surface oxygen and nitrogen functional groups, ionized PMS and AO7 molecules can be anchored to the surface of the catalyst and activated. Duan et al. [65] reported that N-doping even a low ratio (0.8%) can significantly enhance the organic pollution degradation through PMS activation and entirely alter the oxidative pathway from radical to non-radical process. Table S2 shows that the N atomic ratio in ASMn-Nb is 3.9% while the graphitic and Pyridinic N are 1.3 and 0.8%, respectively. It is well known that Pyridinic N

facilitated reactant adsorption to the adjacent carbon by decreasing the energy barrier and accelerate rate-limiting first-electron shuttling [52]. On the other hand, graphitic N, especially if two graphitic N in the same hexagon, leads to non-uniform electron distribution which can increase the catalytic activity of the composite [66]. Thus, it is rational to deduce that the N atom of ASMn-Nb shuttle electron from the adjacent carbon and produce positively charged carbon. Consequently, the superoxide (electron acceptor) shows a strong affinity to bond with positively charged carbon adjacent to N atoms (PMS-carbon) and acted as a catalytically reactive site or surface-confined radicals instead of realizing SO $_4^{\cdot-}$ instantly (Fig. 7a) [20]. Subsequently, the PMS-carbon oxidize adsorbed AO7 via electron abstraction through sp 2 carbon or inner sphere interaction (PMS-AO7). The O1 s XPS spectrum of fresh and spent samples shows that the C-O bond in the spent samples increases significantly, which should be corresponding to the sorption of superoxide onto the positive carbon atom (Fig. S13a). The surface carbonyl group also believed to be chemically reactive for producing SO $_4^{\cdot-}$ [20]. However, the ratio of C=O in the entire catalysts was almost similar, but their catalytic efficiency was different (Table S2). For

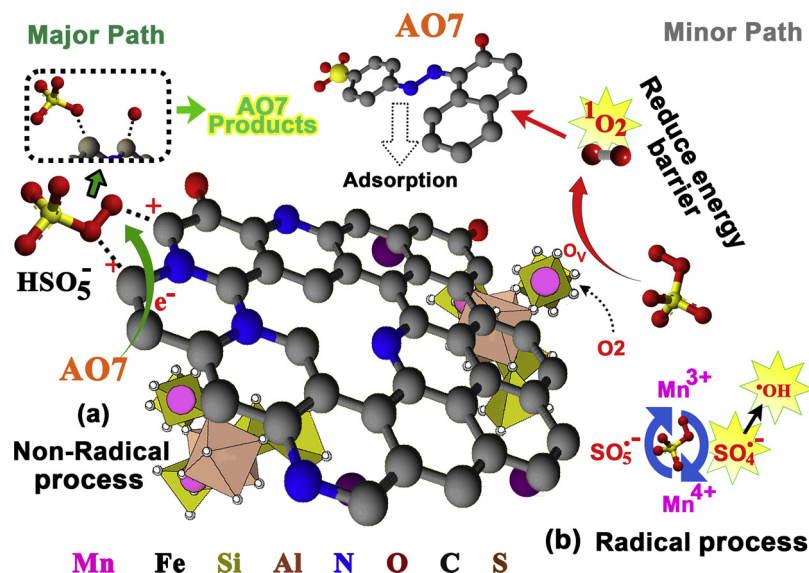
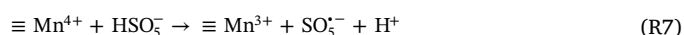
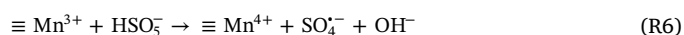
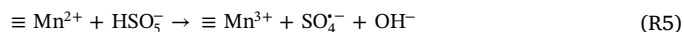


Fig. 7. proposed mechanisms of PMS decomposition over ASMn-Nb and subsequent degradation of AO7.

instance, Sb shows only 16% AO7 removal efficiency in 1 h, which evidence that the catalysis induced by carbonyl group was inadequate compared to other processes in this study. Previous studies reported that PMS only cleaved to $\text{SO}_4^{\cdot-}$ over carbonyl groups of carbon clusters [20], and produced $\text{SO}_4^{\cdot-}$ and $\cdot\text{OH}$ by MnO_x redox cycling [23,24]. Hence, the production of $^1\text{O}_2$ can be ascribed to some oxygen defects of ASMn-Nb. The defective oxygen can adsorb dissolve oxygen (DO) from the media and acted as catalytically active sites for producing $^1\text{O}_2$ by trapping PMS activation energy [6,67]. Fig. S12b shows that the DO concentration reduced rapidly at the first 10 min of reaction, indicating the sorption of DO onto the oxygen defects. After 15 min, DO concentration increase slightly which ascribed to the production of $^1\text{O}_2$. Furthermore, the O1s XPS spectrum of the spent sample shows a significant elevation at 631.36 eV than that of the fresh sample, which confirms the involvement of defected oxygen in catalysis (Fig. S13a). The DO concentration in the reaction media also evidence that singlet oxygenation was not the primary mechanisms of AO7 degradation [67]. The MnO_x of catalyst performed $\text{Mn}^{2+}/\text{Mn}^{3+}$ and $\text{Mn}^{3+}/\text{Mn}^{4+}$ redox cycling as shown in reactions R5–R8 for the production of $\text{SO}_4^{\cdot-}$ and $\cdot\text{OH}$. Therefore, the ratio of different Mn oxidation states has changed in the spent samples (Fig. S13b). Another important characteristic of ASMn-Nb that obviously contribute to enhance catalytic performance is its high surface area and microporosity. Due to the high surface area, more reactants can reach to catalyst surface, while the porous structure can diffuse them to the catalytically active sites. Thus, the catalytic reaction was conducted rapidly. Combining the advantages of rich N-atoms, MnO_x , oxygen defects, and large surface and porous structure, ASMn-Nb shows superior catalytic performance than other as-synthesized catalysts.



4. Conclusion

This study demonstrates that the catalytic performance of simple sludge biochar can be significantly improved by conditioning with MnCl_2 and NH_4OH activation. Sample characterization shows that mixed valent Mn oxides successfully formed on the hybrid sludge

catalyst (ASMn-Nb), while NH_4OH treatment enhanced N atoms, surface areas, and porosity. By using the catalyst to activate PMS for AO7 degradation, complete removal can be achieved within 40 min in a wide range of pH, while non-modified sludge biochar achieved only 16%. Both non-radical (primary) and radical (secondary) process governing PMS activation and subsequent AO7 degradation, whereas N-carbon acted as main and MnO_x , oxygen defects, and carbonyl groups acted as secondary reactive sites. The catalyst was recyclable and shows negligible metal leaching after catalytic reactions. This work concurrently provides an efficient way of heterogeneous PMS activation route and an alternative of conventional sludge disposal method which may be open a new wing towards sludge valorization.

Acknowledgments

The authors acknowledge the support from the National Natural Science Foundation of China (NO. 41173032) and Key Program for Science and Technology Development of Anhui Province (No. 1804b06020358). We acknowledge editors and reviewers for polishing the language of the paper and for in-depth discussion

Appendix A. Supplementary data

Supplementary material related to this article can be found, in the online version, at doi:<https://doi.org/10.1016/j.apcatb.2019.117765>.

References

- [1] C. Wang, J. Kang, P. Liang, H. Zhang, H. Sun, M.O. Tade, S. Wang, Ferric carbide nanocrystals encapsulated in nitrogen-doped carbon nanotubes as an outstanding environmental catalyst, *Environ. Sci. Nano* 4 (2017) 170–179, <https://doi.org/10.1039/C6EN00397D>.
- [2] A. Outsouk, Z. Frontistis, R.S. Ribeiro, M. Antonopoulou, I.K. Konstantinou, A.M.T. Silva, J.L. Faria, H.T. Gomes, D. Mantzavinos, Activation of sodium persulfate by magnetic carbon xerogels (CX/CoFe) for the oxidation of bisphenol A: process variables effects, matrix effects and reaction pathways, *Water Res.* 124 (2017) 97–107, <https://doi.org/10.1016/j.watres.2017.07.046>.
- [3] T. Zeng, M. Yu, H. Zhang, Z. He, J. Chen, S. Song, Fe/Fe3C@N-doped porous carbon hybrids derived from nano-scale MOFs: robust and enhanced heterogeneous catalyst for peroxymonosulfate activation, *Catal. Sci. Technol.* 7 (2017) 396–404, <https://doi.org/10.1039/C6CY02130A>.
- [4] Q. Peng, Y. Ding, L. Zhu, G. Zhang, H. Tang, Fast and complete degradation of norfloxacin by using Fe/Fe3C@NG as a bifunctional catalyst for activating peroxymonosulfate, *Sep. Purif. Technol.* 202 (2018) 307–317, <https://doi.org/10.1016/j.seppur.2018.03.049>.
- [5] Y. Ren, L. Lin, J. Ma, J. Yang, J. Feng, Z. Fan, Sulfate radicals induced from peroxymonosulfate by magnetic ferrosilicate MFe2O4 (M = Co, Cu, Mn, and Zn) as

- heterogeneous catalysts in the water, *Appl. Catal. B Environ.* 165 (2015) 572–578, <https://doi.org/10.1016/j.apcatb.2014.10.051>.
- [6] X. Tian, P. Gao, Y. Nie, C. Yang, Z. Zhou, Y. Li, Y. Wang, A novel singlet oxygen involved peroxymonosulfate activation mechanism for degradation of ofloxacin and phenol in water, *Chem. Commun.* 53 (2017) 6589–6592, <https://doi.org/10.1039/C7CC02820B>.
 - [7] P. Liang, C. Zhang, X. Duan, H. Sun, S. Liu, M.O. Tade, S. Wang, N-Doped graphene from metal-organic frameworks for catalytic oxidation of p-hydroxybenzoic acid: N-functionality and mechanism, *ACS Sustain. Chem. Eng.* 5 (2017) 2693–2701, <https://doi.org/10.1021/acssuschemeng.6b03035>.
 - [8] J. Fan, H. Qin, S. Jiang, Mn-doped g-C₃N₄ composite to activate peroxymonosulfate for acetaminophen degradation: The role of superoxide anion and singlet oxygen, *Chem. Eng. J.* 359 (2019) 723–732, <https://doi.org/10.1016/j.cej.2018.11.165>.
 - [9] L.W. Matzek, K.E. Carter, Activated persulfate for organic chemical degradation: a review, *Chemosphere* 151 (2016) 178–188, <https://doi.org/10.1016/j.chemosphere.2016.02.055>.
 - [10] J. Wang, S. Wang, Activation of persulfate (PS) and peroxymonosulfate (PMS) and application for the degradation of emerging contaminants, *Chem. Eng. J.* 334 (2018) 1502–1517, <https://doi.org/10.1016/j.cej.2017.11.059>.
 - [11] B.-C. Huang, J. Jiang, G.-X. Huang, H.-Q. Yu, Sludge biochar-based catalysts for improved pollutant degradation by activating peroxymonosulfate, *J. Mater. Chem. A* 6 (2018) 8978–8985, <https://doi.org/10.1039/C8TA02282H>.
 - [12] H. Sun, X. Yang, L. Zhao, T. Xu, J. Lian, One-pot hydrothermal synthesis of octahedral CoFe/CoFe₂O₄ submicron composite as heterogeneous catalysts with enhanced peroxymonosulfate activity, *J. Mater. Chem. A* 4 (2016) 9455–9465, <https://doi.org/10.1039/C6TA02126C>.
 - [13] E.-T. Yun, J.H. Lee, J. Kim, H.-D. Park, J. Lee, Identifying the nonradical mechanism in the peroxymonosulfate activation process: singlet oxygenation versus mediated electron transfer, *Environ. Sci. Technol.* 52 (2018) 7032–7042, <https://doi.org/10.1021/acs.est.8b00959>.
 - [14] E.-T. Yun, H.-Y. Yoo, H. Bae, H.-I. Kim, J. Lee, Exploring the role of persulfate in the activation process: radical precursor versus electron acceptor, *Environ. Sci. Technol.* 51 (2017) 10090–10099, <https://doi.org/10.1021/acs.est.7b02519>.
 - [15] E.-T. Yun, G.-H. Moon, H. Lee, T.H. Jeon, C. Lee, W. Choi, J. Lee, Oxidation of organic pollutants by peroxymonosulfate activated with low-temperature-modified nanodiamonds: Understanding the reaction kinetics and mechanism, *Appl. Catal. B Environ.* 237 (2018) 432–441, <https://doi.org/10.1016/j.apcatb.2018.04.067>.
 - [16] H. Lee, H.-J. Lee, J. Jeong, J. Lee, N.-B. Park, C. Lee, Activation of persulfates by carbon nanotubes: oxidation of organic compounds by nonradical mechanism, *Chem. Eng. J.* 266 (2015) 28–33, <https://doi.org/10.1016/j.cej.2014.12.065>.
 - [17] P. Liang, C. Zhang, X. Duan, H. Sun, S. Liu, M.O. Tade, S. Wang, An insight into metal organic framework derived N-doped graphene for the oxidative degradation of persistent contaminants: formation mechanism and generation of singlet oxygen from peroxymonosulfate, *Environ. Sci. Nano* 4 (2017) 315–324, <https://doi.org/10.1039/C6EN00633G>.
 - [18] C.-X. Li, C.-B. Chen, J.-Y. Lu, S. Cui, J. Li, H.-Q. Liu, W.-W. Li, F. Zhang, Metal organic framework-derived CoMn₂O₄ catalyst for heterogeneous activation of peroxymonosulfate and sulfanilamide degradation, *Chem. Eng. J.* 337 (2018) 101–109, <https://doi.org/10.1016/j.cej.2017.12.069>.
 - [19] X. Duan, H. Sun, Z. Shao, S. Wang, Nonradical reactions in environmental remediation processes: uncertainty and challenges, *Appl. Catal. B Environ.* 224 (2018) 973–982, <https://doi.org/10.1016/j.apcatb.2017.11.051>.
 - [20] X. Duan, H. Sun, S. Wang, Metal-free photocatalysis in advanced oxidation reactions, *Acc. Chem. Res.* 51 (2018) 678–687, <https://doi.org/10.1021/acs.accounts.7b00535>.
 - [21] Y.-Y. Ahn, H. Bae, H.-I. Kim, S.-H. Kim, J.-H. Kim, S.-G. Lee, J. Lee, Surface-loaded metal nanoparticles for peroxymonosulfate activation: efficiency and mechanism reconnaissance, *Appl. Catal. B Environ.* 241 (2019) 561–569, <https://doi.org/10.1016/j.apcatb.2018.09.056>.
 - [22] S. Luo, L. Duan, B. Sun, M. Wei, X. Li, A. Xu, Manganese oxide octahedral molecular sieve (OMS-2) as an effective catalyst for degradation of organic dyes in aqueous solutions in the presence of peroxymonosulfate, *Appl. Catal. B Environ.* 164 (2015) 92–99, <https://doi.org/10.1016/j.apcatb.2014.09.008>.
 - [23] M. Wang, Y. Wei, Q. Zou, W. Zhang, A. Xu, X. Li, Tuning manganese (III) species in manganese oxide octahedral molecular sieve by interaction with carbon nanofibers for enhanced pollutant degradation in the presence of peroxymonosulfate, *J. Colloid Interface Sci.* 536 (2019) 271–280, <https://doi.org/10.1016/j.jcis.2018.10.055>.
 - [24] Y. Yao, Y. Cai, F. Lu, F. Wei, X. Wang, S. Wang, Magnetic recoverable MnFe₂O₄ and MnFe₂O₄-graphene hybrid as heterogeneous catalysts of peroxymonosulfate activation for efficient degradation of aqueous organic pollutants, *J. Hazard. Mater.* 270 (2014) 61–70, <https://doi.org/10.1016/j.jhazmat.2014.01.027>.
 - [25] Y. Wang, S. Indrawirawan, X. Duan, H. Sun, H.M. Ang, M.O. Tade, S. Wang, New insights into heterogeneous generation and evolution processes of sulfate radicals for phenol degradation over one-dimensional α -MnO₂ nanostructures, *Chem. Eng. J.* 266 (2015) 12–20, <https://doi.org/10.1016/j.cej.2014.12.066>.
 - [26] E. Saputra, S. Muhammad, H. Sun, H.-M. Ang, M.O. Tade, S. Wang, Shape-controlled activation of peroxymonosulfate by single crystal α -Mn₂O₃ for catalytic phenol degradation in aqueous solution, *Appl. Catal. B Environ.* 154–155 (2014) 246–251, <https://doi.org/10.1016/j.apcatb.2014.02.026>.
 - [27] E. Saputra, S. Muhammad, H. Sun, H.M. Ang, M.O. Tade, S. Wang, Different crystallographic one-dimensional MnO₂ nanomaterials and their superior performance in catalytic phenol degradation, *Environ. Sci. Technol.* 47 (2013) 5882–5887, <https://doi.org/10.1021/es400878c>.
 - [28] M.M. Mian, G. Liu, B. Fu, Conversion of sewage sludge into environmental catalyst and microbial fuel cell electrode material: a review, *Sci. Total Environ.* 666 (2019) 525–539, <https://doi.org/10.1016/j.scitotenv.2019.02.200>.
 - [29] X. Wang, L. Gu, P. Zhou, N. Zhu, C. Li, H. Tao, H. Wen, D. Zhang, Pyrolytic temperature dependent conversion of sewage sludge to carbon catalyst and their performance in persulfate degradation of 2-Naphthol, *Chem. Eng. J.* 324 (2017) 203–215, <https://doi.org/10.1016/j.cej.2017.04.101>.
 - [30] S. Wang, J. Wang, Activation of peroxymonosulfate by sludge-derived biochar for the degradation of triclosan in water and wastewater, *Chem. Eng. J.* 356 (2019) 350–358, <https://doi.org/10.1016/j.cej.2018.09.062>.
 - [31] M.M. Mian, G. Liu, Sewage sludge-derived TiO₂/Fe/Fe₃C-biochar composite as an efficient heterogeneous catalyst for degradation of methylene blue, *Chemosphere* 215 (2019) 101–114, <https://doi.org/10.1016/j.chemosphere.2018.10.027>.
 - [32] S.-J. Yuan, X.-W. Li, X.-H. Dai, Efficient degradation of organic pollutants with a sewage sludge support and in situ doped TiO₂ under visible light irradiation conditions, *RSC Adv.* 4 (2014) 61036–61044, <https://doi.org/10.1039/C4RA12434K>.
 - [33] Y. Huang, Y. Sun, Z. Xu, M. Luo, C. Zhu, L. Li, Removal of aqueous oxalic acid by heterogeneous catalytic ozonation with MnOx/sewage sludge-derived activated carbon as catalysts, *Sci. Total Environ.* 575 (2017) 50–57, <https://doi.org/10.1016/j.scitotenv.2016.10.026>.
 - [34] J. Ji, X. Li, J. Xu, X. Yang, H. Meng, Z. Yan, Zn-Fe-rich granular sludge carbon (GSC) for enhanced electrocatalytic removal of bisphenol A (BPA) and Rhodamine B (RhB) in a continuous-flow three-dimensional electrode reactor (3DER), *Electrochim. Acta* 284 (2018) 587–596, <https://doi.org/10.1016/j.electacta.2018.07.203>.
 - [35] Y. Jia, H. Feng, D. Shen, Y. Zhou, T. Chen, M. Wang, W. Chen, Z. Ge, L. Huang, S. Zheng, High-performance microbial fuel cell anodes obtained from sewage sludge mixed with fly ash, *J. Hazard. Mater.* 354 (2018) 27–32, <https://doi.org/10.1016/j.jhazmat.2018.04.008>.
 - [36] G. Wen, Z.-H. Pan, J. Ma, Z.-Q. Liu, L. Zhao, J.-J. Li, Reuse of sewage sludge as a catalyst in ozonation—efficiency for the removal of oxalic acid and the control of bromate formation, *J. Hazard. Mater.* 239–240 (2012) 381–388, <https://doi.org/10.1016/j.jhazmat.2012.09.016>.
 - [37] C. Marinescu, M. Ben Ali, A. Hamdi, Y. Cherifi, A. Barras, Y. Coffinier, S. Somacescu, V. Raditoiu, S. Zuneris, R. Boukherroub, Cobalt phthalocyanine-supported reduced graphene oxide: a highly efficient catalyst for heterogeneous activation of peroxymonosulfate for rhodamine B and pentachlorophenol degradation, *Chem. Eng. J.* 336 (2018) 465–475, <https://doi.org/10.1016/j.cej.2017.12.009>.
 - [38] J. Chen, L. Zhang, T. Huang, W. Li, Y. Wang, Z. Wang, Decolorization of azo dye by peroxymonosulfate activated by carbon nanotube: radical versus non-radical mechanism, *J. Hazard. Mater.* 320 (2016) 571–580, <https://doi.org/10.1016/j.jhazmat.2016.07.038>.
 - [39] M.M. Mian, G. Liu, B. Yousaf, B. Fu, H. Ullah, M.U. Ali, Q. Abbas, M.A. Mujtaba Munir, L. Ruijia, Simultaneous functionalization and magnetization of biochar via NH₃ ambient pyrolysis for efficient removal of Cr (VI), *Chemosphere* 208 (2018) 712–721, <https://doi.org/10.1016/j.chemosphere.2018.06.021>.
 - [40] C. Liang, C.-F. Huang, N. Mohanty, R.M. Kurakalva, A rapid spectrophotometric determination of persulfate anion in ISCO, *Chemosphere* 73 (2008) 1540–1543, <https://doi.org/10.1016/j.chemosphere.2008.08.043>.
 - [41] C.A. Eveleens, Y. Hijikata, S. Irlé, A.J. Page, Chiral-selective carbon nanotube etching with ammonia: a quantum chemical investigation, *J. Phys. Chem. C* 120 (2016) 19862–19870, <https://doi.org/10.1021/acs.jpcc.6b06997>.
 - [42] M.M. Mian, G. Liu, Recent progress in biochar-supported photocatalysts: synthesis, role of biochar, and applications, *RSC Adv.* 8 (2018), <https://doi.org/10.1039/c8ra02258e>.
 - [43] Ihsanullah, A.M. Al Amer, T. Laoui, A. Abbas, N. Al-Aqeeli, F. Patel, M. Khraisheh, M.A. Atieh, N. Hilal, Fabrication and antifouling behaviour of a carbon nanotube membrane, *Mater. Des.* 89 (2016) 549–558, <https://doi.org/10.1016/j.matdes.2015.10.018>.
 - [44] S. Rehman, T. Tang, Z. Ali, X. Huang, Y. Hou, Integrated design of MnO₂/Carbon hollow nanoboxes to synergistically encapsulate polysulfides for empowering lithium sulfur batteries, *Small* 13 (2017) 1700087, <https://doi.org/10.1002/sml.201700087>.
 - [45] M.M. Mian, G. Liu, B. Yousaf, B. Fu, R. Ahmed, Q. Abbas, M.A.M. Munir, L. Ruijia, One-step synthesis of N-doped metal/biochar composite using NH₃ - ambient pyrolysis for efficient degradation and mineralization of methylene blue, *J. Environ. Sci.* (2018), <https://doi.org/10.1016/j.jes.2018.06.014>.
 - [46] D.K. Padhi, K. Parida, Facile fabrication of α -FeOOH nanorod/RGO composite: a robust photocatalyst for reduction of Cr(VI) under visible light irradiation, *J. Mater. Chem. A* 2 (2014) 10300–10312, <https://doi.org/10.1039/C4TA00931B>.
 - [47] A.A. Dubale, W.-N. Su, A.G. Tamirat, C.-J. Pan, B.A. Aragaw, H.-M. Chen, C.-H. Chen, B.-J. Hwang, The synergetic effect of graphene on Cu₂O nanowire arrays as a highly efficient hydrogen evolution photocathode in water splitting, *J. Mater. Chem. A* 2 (2014) 18383–18397, <https://doi.org/10.1039/C4TA03464C>.
 - [48] X. Duan, K. O'Donnell, H. Sun, Y. Wang, S. Wang, Sulfur and nitrogen co-doped graphene for metal-free catalytic oxidation reactions, *Small* 11 (2015) 3036–3044, <https://doi.org/10.1002/sml.201403715>.
 - [49] X. Dai, Y. Xu, B. Dong, Effect of the micron-sized silica particles (MSSP) on biogas conversion of sewage sludge, *Water Res.* 115 (2017) 220–228, <https://doi.org/10.1016/j.watres.2017.02.064>.
 - [50] N. Wang, B. Lu, L. Li, W. Niu, Z. Tang, X. Kang, S. Chen, Graphitic nitrogen is responsible for oxygen electroreduction on nitrogen-doped carbons in alkaline electrolytes: insights from activity attenuation studies and theoretical calculations, *ACS Catal.* 8 (2018) 6827–6836, <https://doi.org/10.1021/acscatal.8b00338>.
 - [51] D. Kim, N.P. Zussblatt, H.T. Chung, S.M. Becwar, P. Zelenay, B.F. Chmelka, Highly graphitic mesoporous Fe,N-doped carbon materials for oxygen reduction electrochemical catalysts, *ACS Appl. Mater. Interfaces* 10 (2018) 25337–25349, <https://doi.org/10.1021/acsami.8b06009>.

- [52] J. Shi, Y. Wang, W. Du, Z. Hou, Synthesis of graphene encapsulated Fe₃C in carbon nanotubes from biomass and its catalysis application, *Carbon* N. Y. 99 (2016) 330–337, <https://doi.org/10.1016/j.carbon.2015.12.049>.
- [53] L. Li, J. Luo, Y. Liu, F. Jing, D. Su, W. Chu, Self-propagated flaming synthesis of highly active layered CuO-8-MnO₂ hybrid composites for catalytic total oxidation of toluene pollutant, *ACS Appl. Mater. Interfaces* 9 (2017) 21798–21808, <https://doi.org/10.1021/acsami.7b04380>.
- [54] Y. Zhu, S. Liu, C. Jin, S. Bie, R. Yang, J. Wu, MnOx decorated CeO₂ nanorods as cathode catalyst for rechargeable lithium–air batteries, *J. Mater. Chem. A* 3 (2015) 13563–13567, <https://doi.org/10.1039/C5TA02722E>.
- [55] X. Li, Z. Ao, J. Liu, H. Sun, A.I. Rykov, J. Wang, Topotactic transformation of metal–organic frameworks to graphene-encapsulated transition-metal nitrides as efficient Fenton-like catalysts, *ACS Nano* 10 (2016) 11532–11540, <https://doi.org/10.1021/acsnano.6b07522>.
- [56] R. Miao, J. He, S. Sahoo, Z. Luo, W. Zhong, S.-Y. Chen, C. Guild, T. Jafari, B. Dutta, S.A. Cetegen, M. Wang, S.P. Alpay, S.L. Suib, Reduced graphene oxide supported nickel–manganese–cobalt spinel ternary oxide nanocomposites and their chemically converted sulfide nanocomposites as efficient electrocatalysts for alkaline water splitting, *ACS Catal.* 7 (2017) 819–832, <https://doi.org/10.1021/acscatal.6b02650>.
- [57] B. Hillary, P. Sudarsanam, M.H. Amin, S.K. Bhargava, Nanoscale cobalt–manganese oxide catalyst supported on shape-controlled cerium oxide: effect of nanointerface configuration on structural, redox, and catalytic properties, *Langmuir* 33 (2017) 1743–1750, <https://doi.org/10.1021/acs.langmuir.6b03445>.
- [58] T. Liu, X. Ma, D. Liu, S. Hao, G. Du, Y. Ma, A.M. Asiri, X. Sun, L. Chen, Mn doping of CoP nanosheets array: an efficient electrocatalyst for hydrogen evolution reaction with enhanced activity at All pH values, *ACS Catal.* 7 (2017) 98–102, <https://doi.org/10.1021/acscatal.6b02849>.
- [59] Y.-Y. Ahn, E.-T. Yun, J.-W. Seo, C. Lee, S.H. Kim, J.-H. Kim, J. Lee, Activation of peroxymonosulfate by surface-loaded noble metal nanoparticles for oxidative degradation of organic compounds, *Environ. Sci. Technol.* 50 (2016) 10187–10197, <https://doi.org/10.1021/acs.est.6b02841>.
- [60] C. Qi, X. Liu, J. Ma, C. Lin, X. Li, H. Zhang, Activation of peroxymonosulfate by base: Implications for the degradation of organic pollutants, *Chemosphere* 151 (2016) 280–288, <https://doi.org/10.1016/j.chemosphere.2016.02.089>.
- [61] Y. Yang, G. Banerjee, G.W. Brudvig, J.-H. Kim, J.J. Pignatello, Oxidation of organic compounds in water by unactivated peroxymonosulfate, *Environ. Sci. Technol.* 52 (2018) 5911–5919, <https://doi.org/10.1021/acs.est.8b00735>.
- [62] S. Zhu, X. Li, J. Kang, X. Duan, S. Wang, Persulfate activation on crystallographic manganese oxides: mechanism of singlet oxygen evolution for nonradical selective degradation of aqueous contaminants, *Environ. Sci. Technol.* 53 (2019) 307–315, <https://doi.org/10.1021/acs.est.8b04669>.
- [63] G. Nardi, I. Manet, S. Monti, M.A. Miranda, V. Lhiaubet-Vallet, Scope and limitations of the TEMPO/EPR method for singlet oxygen detection: the misleading role of electron transfer, *Free Radic. Biol. Med.* 77 (2014) 64–70, <https://doi.org/10.1016/j.freeradbiomed.2014.08.020>.
- [64] M. Chen, J.H. Hack, A. Iyer, K.J. Jones, R.L. Opila, Radical-driven silicon surface passivation by benzoquinone- and hydroquinone-methanol and photoinitiators, *J. Phys. Chem. C* 121 (2017) 21364–21373, <https://doi.org/10.1021/acs.jpcc.7b05686>.
- [65] X. Duan, H. Sun, Y. Wang, J. Kang, S. Wang, N-Doping-Induced nonradical reaction on single-walled carbon nanotubes for catalytic phenol oxidation, *ACS Catal.* 5 (2015) 553–559, <https://doi.org/10.1021/cs5017613>.
- [66] G. Wu, K.L. More, P. Xu, H.-L. Wang, M. Ferrandon, A.J. Kropf, D.J. Myers, S. Ma, C.M. Johnston, P. Zelenay, A carbon-nanotube-supported graphene-rich non-precious metal oxygen reduction catalyst with enhanced performance durability, *Chem. Commun.* 49 (2013) 3291–3293, <https://doi.org/10.1039/C3CC39121C>.
- [67] Y. Huang, X. Tian, Y. Nie, C. Yang, Y. Wang, Enhanced peroxymonosulfate activation for phenol degradation over MnO₂ at pH 3.5–9.0 via Cu(II) substitution, *J. Hazard. Mater.* 360 (2018) 303–310, <https://doi.org/10.1016/j.jhazmat.2018.08.028>.